Glucose-Dependent miR-125b Is a Negative Regulator of β-Cell Function

Rebecca Cheung,[1] Grazia Pizza,[1] Pauline Chabosseau,[1] Delphine Rolando,[2] Alejandra Tomas,[1] Thomas Burgoyne,[3] Zhiyi Wu,[1] Anna Salowka,[1] Anusha Thapa,[1] Annabel Macklin,[1] Yufei Cao,[1] Marie-Sophie Nguyen-Tu,[1] Matthew T. Dickerson,[4] David A. Jacobson,[4] Piero Marchetti,[5] James Shapiro,[6] Lorenzo Piemonti,[7] Eelco de Koning,[8] Isabelle Leclerc,[9] Karim Bouzakri,[10] Kei Sakamoto,[11] David M. Smith,[12] Guy A. Rutter,[1,9,13] and Aida Martinez-Sanchez[1]

Diabetes 2022;71:1525–1545 | https://doi.org/10.2337/db21-0803

Impaired pancreatic β-cell function and insulin secretion are hallmarks of type 2 diabetes. miRNAs are short, noncoding RNAs that silence gene expression vital for the development and function of β cells. We have previously shown that β cell–specific deletion of the important energy sensor AMP-activated protein kinase (AMPK) results in increased miR-125b-5p levels. Nevertheless, the function of this miRNA in β cells is unclear. We hypothesized that miR-125b-5p expression is regulated by glucose and that this miRNA mediates some of the deleterious effects of hyperglycemia in β cells. Here, we show that islet miR-125b-5p expression is upregulated by glucose in an AMPK-dependent manner and that short-term miR-125b-5p overexpression impairs glucose-stimulated insulin secretion (GSIS) in the mouse insulinoma MIN6 cells and in human islets. An unbiased, high-throughput screen in MIN6 cells identified multiple miR-125b-5p targets, including the transporter of lysosomal hydrolases *M6pr* and the mitochondrial fission regulator *Mtfp1*. Inactivation of miR-125b-5p in the human β-cell line EndoCβ-H1 shortened mitochondria and enhanced GSIS, whereas mice overexpressing miR-125b-5p selectively in β cells (MIR125B-Tg) were hyperglycemic and glucose intolerant. MIR125B-Tg β cells contained enlarged lysosomal structures and had reduced insulin content and secretion. Collectively, we identify miR-125b as a glucose-controlled regulator of organelle dynamics that modulates insulin secretion.

Pancreatic β cells are essential regulators of glucose homeostasis, secreting insulin in response to increases in circulating levels of the sugar (1). Nevertheless, chronic hyperglycemia has a negative effect on β-cell function and survival, contributing to the development of the type 2 diabetes (T2D) (2).

miRNAs are noncoding RNAs, ∼21 nucleotides, that silence gene expression posttranscriptionally and are essential for endocrine cell development and function (3). Even though β cells contain hundreds of different miRNAs, the function of only a few has been studied in detail.

[1]Section of Cell Biology and Functional Genomics, Department of Metabolism, Digestion and Reproduction, Imperial College London, London, U.K.
[2]Beta Cell Genome Regulation Laboratory, Department of Metabolism, Digestion and Reproduction, Imperial College London, London, U.K.
[3]UCL Institute of Ophthalmology, University College London, London, U.K.
[4]Department of Molecular Physiology and Biophysics, Vanderbilt University, Nashville, TN
[5]Department of Clinical and Experimental Medicine, University of Pisa, Pisa, Italy
[6]Clinical Islet Laboratory and Clinical Islet Transplant Program, University of Alberta, Edmonton, Canada
[7]Vita-Salute San Raffaele University, Milan, Italy
[8]Department of Medicine, Leiden University Medical Center, Leiden, the Netherlands
[9]CR-CHUM, University of Montreal, Montreal, Quebec, Canada
[10]UMR DIATHEC, EA 7294, Centre Européen d'Etude du Diabète, Université de Strasbourg, Fédération de Médecine Translationnelle de Strasbourg, Strasbourg, France
[11]Novo Nordisk Foundation Center for Basic Metabolic Research, University of Copenhagen, Copenhagen, Denmark
[12]Emerging Innovations Unit, Discovery Sciences, R&D, AstraZeneca, Cambridge, U.K.
[13]Lee Kong Chian School of Medicine, Nanyang Technological University, Singapore

Corresponding author: Aida Martinez-Sanchez, a.martinez-sanchez@imperial.ac.uk

Received 4 September 2021 accepted 11 April 2022

This article contains supplementary material online at https://doi.org/10.2337/figshare.19609827.

R.C. and G.P. are co-first authors.

© 2022 by the American Diabetes Association. Readers may use this article as long as the work is properly cited, the use is educational and not for profit, and the work is not altered. More information is available at https://diabetesjournals.org/journals/pages/license.

MiR-125b (miR-125b-5p) is a highly conserved miRNA widely studied in the context of tumorigenesis as an important regulator of cellular differentiation and apoptosis (4). We have previously shown that miR-125b expression increases in islets after β cell–specific deletion of AMP-activated protein kinase (βAMPKdKO) (5), suggesting that AMPK may act as a negative regulator of miR-125b expression. AMPK activity is suppressed acutely in β cells by high glucose levels and lowered in islets from individuals with T2D (6).

These observations led us to hypothesize that inhibition of AMPK in response to high glucose levels would result in islet miR-125b upregulation, which may mediate some of the deleterious effects of hyperglycemia in β cells. Here, we show that high glucose levels increase islet miR-125b expression and that miR-125b has an important negative effect in β-cell function, in vitro and in vivo, by targeting genes involved in regulating lysosomal and mitochondrial function.

RESEARCH DESIGN AND METHODS

Cells and Islets Culture and Transfection

MIN6 and EndoCβ-H1 (7) cells and mouse and human islets were obtained, maintained, and then transfected with Lipofectamine 2000 (ThermoFisher Scientific), as described in Supplementary Research Design and Methods.

CRISPR-Cas9–Mediated Deletion of miR-125b in EndoCβ-H1 Cells

EndoCβ-H1 cells were infected with lentiviral vectors expressing two guide RNAs targeting *MIR125B-2* and a rat insulin promoter (RIP)-driven hSpCas9. Lentivirus without guide RNAs was used as a control. Integrating EndoCβ-H1 cells were selected with puromycin. See Supplementary Research Design and Methods for more details.

Generation of Transgenic Mice

The cassette expressing miR-125b under the control of a reverse tetracycline transactivator (rtTA)-inducible promoter was excised from pBI-LTet-MIR125B and used for pronuclear microinjection of C57BL6/J oocytes at the Centre for Transgenic Models Basel, Switzerland). A founder with a unique copy of the transgene was bred with mice expressing the rtTA under the control of the RIP7 promoter (RIP7-rtTA$^{+/+}$). Mice bearing the transgene (MIR125B-Tg: RIP7-rtTA$^{+/-}$, MIR125B Tg$^{+/-}$) and control (RIP7-rtTA$^{+/-}$) were used in subsequent experiments. Doxycycline (0.5 g/L) was continuously administered in the drinking water from the time of mating. Mice had free access to standard chow or, when indicated, ketogenic diet (Ssniff). In vivo procedures were approved by the UK Home Office Animal Scientific Procedures Act, 1986 (Licenses PA03F7F0F and PP7151519).

RNA Extraction, Reverse Transcription, and Quantitative PCR

Quantitative reverse transcription PCR was performed as previously described (5). For miRNA quantification, let-7d-3p (Figs. 1 and 4) and miR-574-3p (Supplementary Figs. 1 and 2) were used as endogenous controls because of their stable expression in our system (5). For mitochondria DNA to nuclear DNA ratio analysis, islet DNA was extracted with 40 μg/mL proteinase K in SNET buffer.

miRNA Induced Silencing Complex Immunoprecipitation, RNA Sequencing Library Preparation, Sequencing, and Analysis

miRNA induced silencing complex (miRISC) immunoprecipitation was performed as previously described (8) with a mouse–anti–AGO2 antibody (clone E12–1C9; Abnova). Library preparation from mRNA enriched from total RNA with a NEBNext Poly(A) mRNA Magnetic Isolation Kit (New England Biolabs) and from miRISC-isolated RNA was performed using a NEBNext Ultra II Directional RNA Library Prep Kit from Illumina. Library preparation from human islets total RNA (200 ng) was performed using a NEBNext Low Input RNA Library Prep kit (New England Biolabs). Libraries were sequenced on a HiSeq4000. Mapping and differential expression analysis were performed with Salmon v1.3.0 (9) and DESeq2 (10).

For miRNA target identification, total mRNA (T-RNA) and immunoprecipitated RNA (RIP-RNA) samples were treated as separate data sets, and the two resulting gene lists of differential analysis were used to calculate the ratio of RIP-RNA to T-RNA for each gene. Additional details are provided in Supplementary Research Design and Methods.

Immunoblot and Immunohistochemistry

Western immunoblotting was performed with EndoCβ-H1 total protein (5–15 μg) or and extract of 10–20 islets prepared with radioimmunoprecipitation assay. Islets and slides from isolated pancreata for immunohistochemistry were prepared, visualized, and quantified as previously described (11). Additional details on the approaches used for blotting, β-cell mass, proliferation, apoptosis, and cathepsin D/LAMP1 measurements, and an exhaustive list of all antibodies and kits used can be found in Supplementary Research Design and Methods.

Electron Microscopy

MIN6 and EndoCβ-H1 cells and whole isolated islets were fixed and prepared as described by Jones et al. (12). Ultrathin 70 nm sections were examined in Tecnai Spirit or JEOL 1400plus transmission electron microscopes. Images at ×2,000 magnification were analyzed and quantified blindly in ImageJ, as described by Pasquier et al. (13).

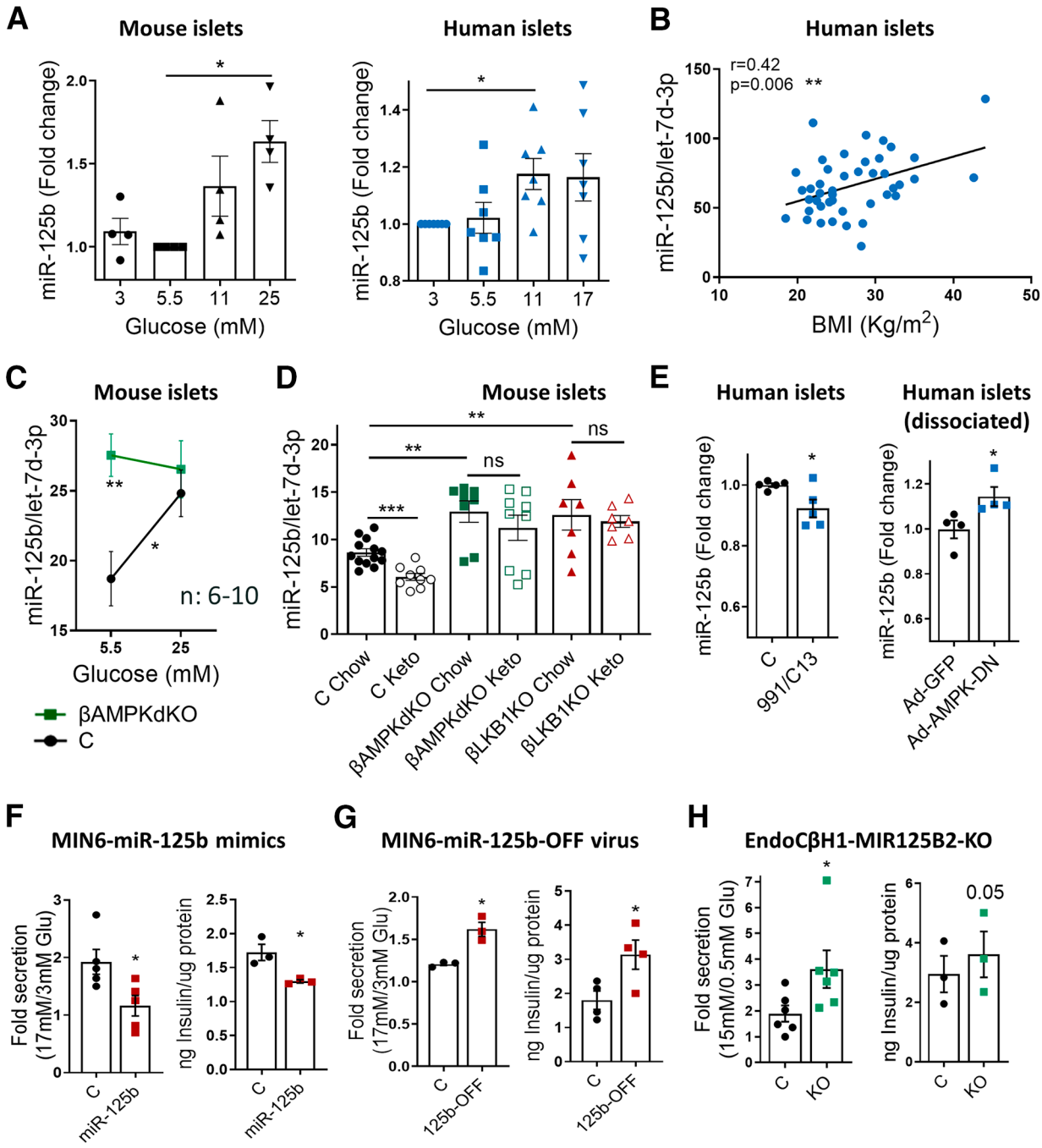

Figure 1—MiR-125b expression is stimulated by glucose via AMPK repression in islets and regulates insulin secretion in insulinoma/β-cell lines. *A–E*: Quantitative RT-PCR measurements of MiR-125b in (*A*) mouse and human islets cultured at the indicated glucose concentrations for 48 h; (*B*) human islets (from nondiabetic donors) kept for 24 h at 5.5 mM glucose plotted against donor's BMI; (*C*) islets from βAMPKdKO (green) and control (C; black) mice cultured at 5.5 or 25 mM glucose for 48 h; (*D*) islets from βAMPKdKO (green), βLKB1KO (red), and control (black) male and female mice fed a chow or a ketogenic (Keto) diet for 28 days; and (*E*) human islets treated with the AMPK activators ^{13}C (50 nM) and C-991 (20 nM) for 16 h (left) and dissociated human islets infected with adenovirus expressing a dominant-negative AMPK protein (Ad-AMPK-DN) or empty control (Ad-GFP) at a multiplicity of infection (MOI) of 5 for 48 h (right). Each dot represents islets from a single mouse or human donor. MiR-125b expression is normalized to that of the endogenous control let-7d-3p (*4*). *F–H*: GSIS (left panels) and insulin content (right panels). GSIS was quantified after 30 min of 17 or 15 mmol/L glucose stimulation following overnight preincubation at 3 mmol/L glucose of MIN6 (*F*, *G*) and EndoCβ-H1 with CRISPR-mediated miR-125b knockout (KO) (*H*). MIN6 cells were transfected with 5 nM miR-125b (125b) or control mimics (*F*) or infected with adenovirus expressing a miR-125b inhibitor (125b-OFF) or a nontargeting control at a MOI of 10 (*G*) 48 h before the experiments. Intracellular protein content was quantified by bicinchoninic acid assay to calculate insulin content per microgram of total protein. Data are presented as fold change of basal level. Each dot represents an independent experiment with two to three technical replicates. Experiments were performed with three different populations of CRISPR-mediated miR-125b KO and control cells. Error bars represent SEM. *$P < 0.05$, **$P < 0.01$, ***$P < 0.001$, one-way ANOVA (repeated measures) and Dunnet multiple comparisons test (*A*), Pearson correlation adjusted by age and sex (*B*), two-way ANOVA (repeated measures) and Bonferroni multiple comparisons test (*C*), unpaired Welch (*D*) and paired Student (*E–H*) *t* test. ns, not significant.

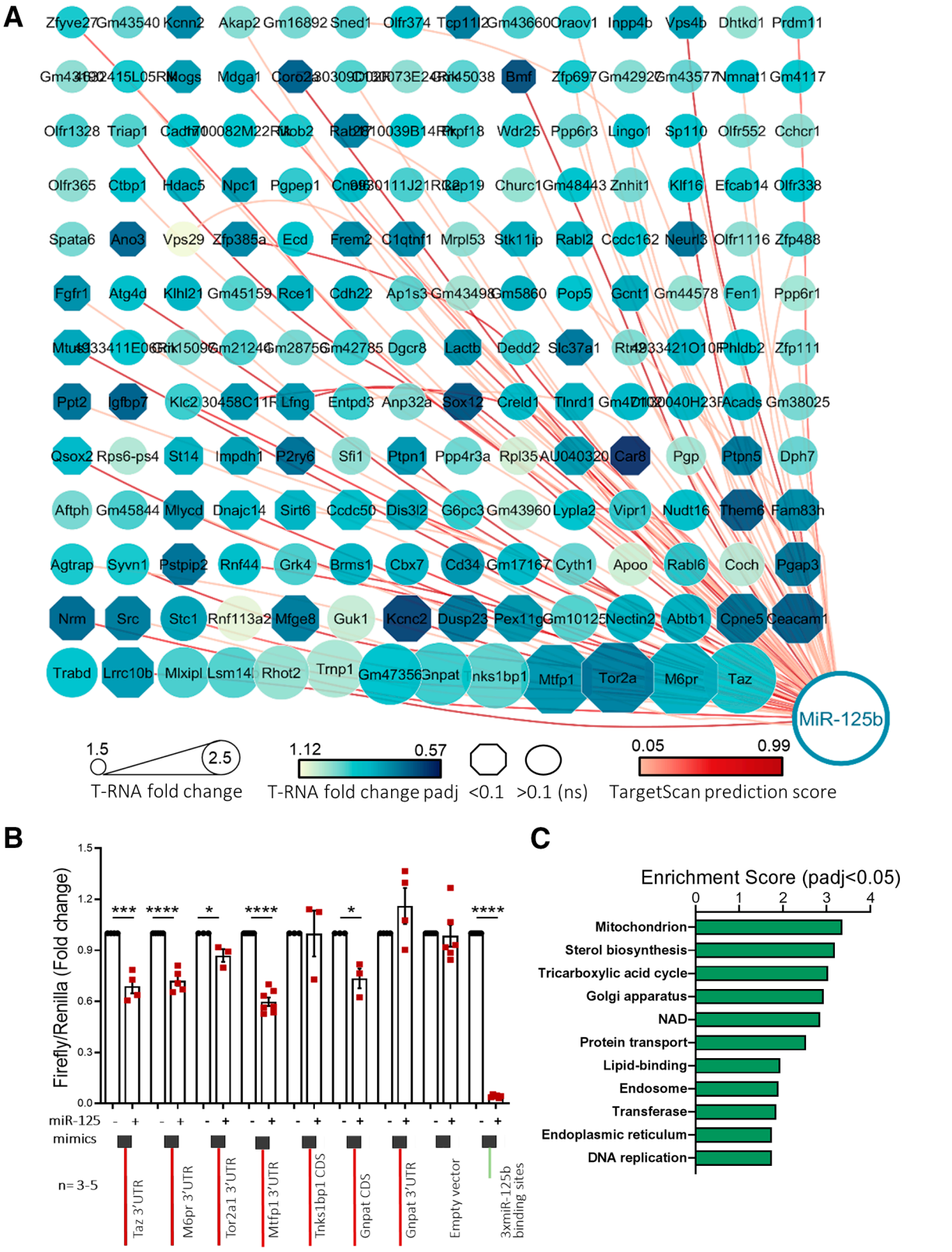

Figure 2—High-through identification and validation of miR-125b target genes. MIN6 cells were transfected with 5 nM control or miR-125b mimics. *A*: Cytoscape-generated (49) layout of genes with RIP-RNA to T-RNA ratio > 1.5 upon miR-125b overexpression (arbitrary cutoff) in MIN6 cells were transfected with 5 nM control or miR-125b mimics. Node size represents the extent of the RIP-RNA to T-RNA ratio (the larger, the higher). The intensity of the gene node color indicates the fold downregulation of each gene upon miR-125b expression (T-RNA). Downregulation at the transcript level was statistically significant for those genes represented in an octagonal shape. Lines connecting the nodes or genes with miR-125b indicate the presence of a predicted binding site for miR-125b as identified by TargetScan,

Intraperitoneal Glucose and Insulin Tolerance Tests and In Vivo Insulin Secretion

Mice fasted overnight (for insulin secretion measurement) or for 5 hours (for insulin tolerance tests) were submitted to intraperitoneal glucose tolerance tests or insulin tolerance tests after administration of 1 g/kg body weight of glucose or 1.2 U/kg insulin (NovoRapid), respectively, as previously described (14). To measure insulin secretion, mice were injected with 3 g/kg glucose and blood insulin levels were measured using an Insulin ELISA kit (Crystal Chem), following manufacturer's instructions.

Insulin Secretion and Content

Cell lines and islets were submitted to glucose- or KCl-stimulated insulin secretion as previously described (7, 14). Secreted and total insulin levels were quantified using an HTRF insulin kit (Cisbio) in a PHERAstar reader (BMG Labtech), following the manufacturer's guidelines. Insulin and protein contents were measured by HTRF and bicinchoninic acid (Pierce), respectively, in radioimmunoprecipitation assay cellular lysates or in full pancreas homogenates, as previously described (11).

Islet Fluorescence Imaging

Ca^{2+} and ATP imaging was performed in whole islets with Cal-520 (4.5 μM; Stratech) and adenovirus-encoded Perceval probe, respectively, and total internal reflection of fluorescence was performed in dissociated islets infected with an adenovirus construct for NPY-Venus, as described by Martinez-Sanchez et al. (14) and Georgiadou et al. (15). Mitochondria morphology analysis was performed with Mitotracker Green (ThermoFisher) as described by Georgiadou et al. (15). See Supplementary Research Design and Methods for additional details.

Whole-Cell Voltage-Clamp Electrophysiology

Voltage-clamp electrophysiology was performed in dissociated β cells using patch electrodes and generating voltage-dependent Ca^{2+}-channel (VDCC) currents by application of sequential 10-mV depolarizing steps as detailed in Supplementary Research Design and Methods.

Extracellular Flux Analysis

Oxygen consumption rate was determined using the XFe96 Extracellular Flux Analyzer and a XFe96 FluxPak (Seahorse Bioscience) in groups of 3–6 size-matched islets per well embedded in Matrigel and incubated at 3 mmol/L glucose followed by 17 mmol/L glucose and oligomycin (5 μmol/L), per manufacturer's instructions.

Statistics

Statistical significance was evaluated with GraphPad Prism 9.0 software, as indicated in the figure legends. Correlation data were estimated using R software with the *ppcor* package (16). All data are shown as mean ± SEM. $P < 0.05$ was considered statistically significant unless otherwise specified.

Study Approval

All mouse in vivo procedures were conducted in accordance with the UK Home Office Animal (Scientific Procedures) Act of 1986 (project license PA03F7F0F to IL) and approved by the Imperial College Animal Welfare and Ethical Review Body. For human islet experiments, islets were isolated from the locations indicated in Supplementary Table 9, with full approval and informed consent.

Data and Resource Availability

All data generated or analyzed during this study are included in the published article and its online supplementary files. No applicable resources were generated or analyzed during this study.

RESULTS

Glucose Stimulates miR-125b Expression via AMPK Repression

To determine whether glucose regulates miR-125b expression in islets, we measured miR-125b in mouse and human islets cultured at increasing glucose concentrations. MiR-125b expression was significantly increased after culture at high (11–25 mM) versus low (3.5–5.5 mmol/L) glucose concentrations (Fig. 1*A*, Supplementary Fig. 1*A*). Consistent with the possible in vivo relevance of these findings, expression of miR-125b in human islets was positively correlated with the BMI of donors but not with their age or sex (Fig. 1*B*, Supplementary Fig. 1*B* and *C*).

Islets from βAMPKdKO mice had significantly higher miR-125b levels than did control islets when cultured at a low (5.5 mM) glucose concentration (Fig. 1*C*, Supplementary Fig. 1*D*), whereas miR-125b expression remained unchanged

with the intensity in the color of the line representing the score (total context score). *B*: Validation of miR-125b binding to the regions (full-length CDS or 3′UTR, as indicated) containing predicted miR-125b binding sites of six identified targets with highest RIP-RNA to T-RNA ratio. Luciferase reporter assay of MIN6 cells cotransfected with pmirGLO plasmids containing the indicated target downstream the luciferase open reading frame and miR-125b (+) or nontargeting (−) control mimics. Samples were measured 24 h after transfection in technical replicates. *Firefly* luciferase values are normalized to *Renilla*, independently expressed by the same vector, and are shown as relative to that obtained for each construct cotransfected with the control miRNA mimic. Each dot represents an independent experiment. A construct containing three perfectly complementary binding sites for miR-125b (positive control) and the empty pmiRGlo vector (negative control) were included in the experiments. *C*: GO enrichment analysis of the genes significantly up- and downregulated upon miR-125b overexpression (T-RNA) and putative miR-125b direct targets (RIP-RNA to T-RNA ratio > 1.5) performed with the Database for Annotation, Visualization and Integrated Discovery. The graph shows enrichment scores for one representative term for each cluster grouped by semantic similarities and including terms with a *P*adj (Benjamini) < 0.05. See Supplementary Table 2 for a full list of terms. Error bars represent SEM. $*P < 0.05$, $***P < 0.001$, $****P < 0.0001$, paired Student *t* test values of the log(fold change) values.

Table 1—miR-125b direct targets identified by integration of RIP-seq and T-RNA sequencing differential analysis.

Gene symbol	Predicted binding-site TargetScan	RNA fold change†	RNA *P*adj†	RIP fold change‡	RIP *P*adj†‡	RIP to RNA ratio
Taz	Y*	0.88	0.213	2.196	0	2.494
M6pr	Y*	0.818	0.006	2.039	0	2.494
Tor2a	Y*	0.722	0.002	1.786	0	2.476
Mtfp1	Y*	0.762	0.018	1.865	0	2.449
Tnks1bp1		0.927	0.607	2.194	0	2.366
Gnpat		0.901	0.44	2.067	0	2.294
Gm47356		0.869	0.602	1.965	0.002	2.262
Trnp1		1.018	0.968	2.201	0	2.163
Rhot2	Y*	0.992	0.982	2.051	0	2.068
Lsm14b		0.924	0.611	1.833	0	1.985
Mlxipl		0.915	0.743	1.812	0	1.981
Lrrc10b	Y*	0.774	0.029	1.521	0.056	1.966
Trabd		0.867	0.416	1.697	0.001	1.957
Ceacam1	Y	0.66	0.002	1.284	0.608	1.944
Cpne5	Y	0.694	0.016	1.345	0.613	1.937
Abtb1	Y*	0.814	0.242	1.576	0.025	1.935
Nectin2		0.821	0.114	1.572	0.05	1.915
Gm10125		0.925	0.818	1.745	0.03	1.886
Pex11g		0.756	0.06	1.419	0.486	1.876
Dusp23	Y	0.703	0.006	1.319	0.768	1.875
Kcnc2	Y*	0.6	0	1.118	0.999	1.864
Guk1		1.045	0.896	1.944	0	1.86
Mfge8	Y	0.712	0.013	1.32	0.771	1.853
Rnf113a2		1.088	0.494	1.998	0.001	1.836
Stc1	Y*	0.785	0.142	1.44	0.406	1.833
Src	Y	0.712	0.011	1.285	0.852	1.804
Nrm	Y*	0.674	0	1.214	0.963	1.801
Pgap3	Y*	0.698	0	1.257	0.802	1.801
Coch		1.027	0.954	1.849	0.004	1.8
Rabl6	Y	0.891	0.331	1.591	0.001	1.786
Apoo		1.059	0.689	1.886	0.004	1.781
Cyth1	Y*	0.94	0.514	1.658	0.001	1.763
Gm17167		0.84	0.445	1.478	0.364	1.758
Cd34	Y*	0.764	0.123	1.34	0.662	1.753
Cbx7	Y*	0.817	0.13	1.431	0.379	1.753
Brms1	Y*	0.826	0.11	1.446	0.428	1.75
Grk4		0.914	0.787	1.597	0.175	1.746
Rnf44	Y*	0.849	0.338	1.478	0.025	1.741
Pstpip2		0.691	0.002	1.203	0.999	1.74
Syvn1	Y*	0.886	0.393	1.54	0	1.738
Agtrap	Y*	0.891	0.601	1.547	0.258	1.737
Fam83h	Y*	0.738	0.001	1.278	0.543	1.732
Them6	Y*	0.649	0.001	1.123	0.999	1.731
Nudt16		0.849	0.234	1.467	0.402	1.728
Vipr1	Y	0.893	0.499	1.541	0	1.726

Continued on p. 1531

Table 1—Continued

Gene symbol	Predicted binding-site TargetScan	RNA fold change†	RNA *P*adj†	RIP fold change‡	RIP *P*adj†‡	RIP to RNA ratio
Lypla2	Y*	0.874	0.204	1.501	0.037	1.718
Gm43960		1.035	0.938	1.767	0.029	1.707
G6pc3		0.9	0.517	1.532	0.114	1.703
Dis3l2	Y*	0.805	0.012	1.367	0.64	1.699
Ccdc50		0.841	0.073	1.429	0.233	1.698
Sirt6	Y*	0.82	0.019	1.386	0.607	1.692
Dnajc14	Y*	0.834	0.002	1.403	0.329	1.683
Mlycd	Y*	0.754	0.002	1.267	0.775	1.681
Gm45844		0.913	0.75	1.53	0.196	1.676
Aftph		0.956	0.747	1.597	0.018	1.671
Dph7		0.941	0.774	1.571	0.209	1.669
Ptpn5		0.706	0.011	1.176	0.999	1.666
Pgp	Y*	1.01	0.98	1.682	0.004	1.665
Car8		0.58	0	0.965	0.999	1.664
AU040320	Y	0.769	0	1.274	0.533	1.656
Rpl35		1.06	0.839	1.75	0.003	1.651
Ppp4r3a	Y	0.95	0.789	1.564	0.003	1.646
Ptpn1	Y*	0.759	0	1.248	0.805	1.645
Sfi1		0.984	0.954	1.615	0.146	1.642
P2ry6		0.687	0	1.127	0.999	1.641
Impdh1		0.785	0.003	1.286	0.379	1.639
St14	Y	0.811	0.087	1.327	0.752	1.636
Rps6-ps4		1.021	0.957	1.668	0.078	1.633
Qsox2	Y*	0.832	0.026	1.357	0.096	1.632
Gm38025		0.957	0.89	1.561	0.243	1.631
Acads	Y*	0.823	0.183	1.342	0.441	1.629
D130040H23Rik	Y	0.828	0.28	1.348	0.673	1.628
Gm47102		0.837	0.442	1.361	0.428	1.626
Tlnrd1		0.809	0.097	1.315	0.533	1.626
Creld1	Y	0.838	0.189	1.36	0.517	1.623
Sox12	Y*	0.639	0	1.036	0.999	1.622
Anp32a		0.963	0.908	1.559	0.006	1.619
Entpd3	Y*	0.903	0.604	1.456	0.078	1.613
Lfng	Y*	0.767	0.075	1.236	0.845	1.613
6030458C11Rik	Y	0.764	0	1.228	0.684	1.608
Klc2	Y*	0.903	0.536	1.45	0.11	1.606
Igfbp7		0.66	0.002	1.059	0.999	1.604
Ppt2	Y	0.69	0	1.106	0.999	1.603
Zfp111	Y	0.958	0.842	1.534	0.111	1.601
Phldb2	Y	0.86	0.455	1.377	0.375	1.6
4933421O10Rik		0.818	0.035	1.307	0.8	1.598
Rtn2		0.966	0.896	1.544	0.037	1.597
Slc37a1		0.702	0	1.12	0.999	1.596
Dedd2		0.899	0.682	1.431	0.286	1.592

Continued on p. 1532

Table 1—Continued

Gene symbol	Predicted binding-site TargetScan	RNA fold change†	RNA *P*adj†	RIP fold change‡	RIP *P*adj†‡	RIP to RNA ratio
Lactb	Y	0.751	0.027	1.195	0.999	1.59
Dgcr8		0.917	0.618	1.459	0.375	1.59
Dgcr8		0.917	0.618	1.459	0.375	1.59
Gm42785		0.902	0.612	1.433	0.379	1.589
Gm28756		0.955	0.912	1.515	0.303	1.587
Gm21244		0.917	0.763	1.455	0.39	1.587
Gm15097		0.967	0.939	1.535	0.258	1.586
4933411E06Rik		0.876	0.62	1.389	0.502	1.585
Mtus1	Y*	0.794	0.052	1.259	0.917	1.584
Ppp6r1		1.011	0.96	1.601	0.001	1.584
Fen1		0.906	0.534	1.434	0.072	1.583
Gm44578		0.989	0.984	1.564	0.229	1.582
Gcnt1	Y*	0.799	0.044	1.263	0.501	1.581
Pop5	Y	0.867	0.448	1.37	0.243	1.581
Gm5860		0.81	0.262	1.278	0.828	1.579
Gm43498		1.005	0.994	1.585	0.183	1.578
Ap1s3	Y*	0.927	0.705	1.462	0.39	1.577
Cdh22	Y	0.808	0.18	1.274	0.666	1.576
Rce1		0.809	0.081	1.275	0.69	1.576
Gm45159		0.926	0.82	1.459	0.398	1.576
Klhl21	Y*	0.829	0.286	1.306	0.693	1.576
Atg4d	Y*	0.843	0.405	1.329	0.613	1.576
Fgfr1	Y*	0.747	0.012	1.175	0.999	1.574
Zfp488	Y	0.924	0.734	1.454	0.428	1.574
Olfr1116		0.982	0.969	1.543	0.258	1.572
Neurl3		0.691	0.005	1.086	0.999	1.571
Ccdc162		0.869	0.499	1.365	0.582	1.57
Rabl2	Y	0.82	0.098	1.287	0.878	1.569
Stk11ip		0.801	0.002	1.255	0.9	1.568
Mrpl53		0.981	0.958	1.538	0.105	1.567
C1qtnf1	Y	0.729	0.024	1.143	0.999	1.567
Frem2		0.739	0.05	1.159	0.999	1.567
Ecd		0.859	0.153	1.346	0.49	1.567
Zfp385a	Y	0.735	0.01	1.15	0.999	1.565
Vps29	Y	1.106	0.536	1.73	0.001	1.564
Ano3		0.673	0.008	1.053	0.999	1.564
Spata6		0.958	0.869	1.494	0.358	1.56
Olfr338		0.866	0.549	1.35	0.603	1.559
Efcab14	Y*	0.887	0.301	1.382	0.364	1.559
Klf16	Y*	0.863	0.152	1.345	0.594	1.559
Znhit1	Y	0.959	0.885	1.492	0.353	1.556
Gm48443		0.875	0.404	1.361	0.533	1.556
Churc1		0.993	0.986	1.545	0.234	1.555
Cep19		0.899	0.523	1.397	0.533	1.554

Continued on p. 1533

Table 1—Continued

Gene symbol	Predicted binding-site TargetScan	RNA fold change†	RNA *P*adj†	RIP fold change‡	RIP *P*adj†‡	RIP to RNA ratio
9930111J21Rik2	Y	0.914	0.785	1.421	0.375	1.554
Cnot6		0.83	0.168	1.289	0.144	1.553
Pgpep1	Y*	0.894	0.61	1.384	0.385	1.548
Npc1		0.771	0.001	1.193	0.977	1.547
Hdac5		0.809	0.151	1.25	0.942	1.544
Ctbp1	Y	0.848	0.005	1.303	0.43	1.537
Olfr365		0.979	0.954	1.505	0.353	1.537
Cchcr1		0.981	0.936	1.507	0.328	1.536
Olfr552		0.967	0.94	1.485	0.345	1.536
Sp110		0.871	0.609	1.337	0.648	1.535
Lingo1	Y	0.852	0.312	1.308	0.474	1.535
Ppp6r3	Y*	0.939	0.618	1.438	0.023	1.531
Wdr25	Y	0.9	0.551	1.377	0.533	1.53
Prpf18		0.907	0.322	1.386	0.443	1.528
2810039B14Rik		0.871	0.496	1.33	0.708	1.528
Rab17	Y	0.718	0.005	1.097	0.999	1.528
Mob2	Y	0.889	0.391	1.355	0.486	1.525
1700082M22Rik		0.874	0.62	1.333	0.717	1.525
Cadm1		0.872	0.385	1.33	0.366	1.525
Triap1	Y*	0.923	0.687	1.408	0.382	1.524
Olfr1328		0.915	0.715	1.394	0.366	1.523
Gm4117		0.878	0.609	1.337	0.639	1.523
Nmnat1	Y	0.852	0.408	1.297	0.819	1.523
Gm43577		0.94	0.864	1.431	0.465	1.523
Gm42927		0.972	0.941	1.479	0.328	1.522
Zfp697	Y	0.888	0.597	1.35	0.689	1.519
Bmf	Y*	0.623	0	0.946	0.999	1.519
Gm45038		0.93	0.795	1.412	0.401	1.518
C130073E24Rik		0.979	0.963	1.487	0.36	1.518
E130309D02Rik	Y	0.924	0.716	1.4	0.366	1.516
Coro2a	Y*	0.656	0	0.994	0.999	1.514
Mdga1	Y*	0.794	0.193	1.201	0.999	1.513
Mogs		0.772	0.05	1.167	0.857	1.512
4632415L05Rik	Y	0.886	0.414	1.339	0.713	1.511
Gm43190		0.978	0.96	1.477	0.375	1.511
Prdm11	Y	0.907	0.683	1.369	0.648	1.51
Dhtkd1		0.991	0.986	1.496	0.345	1.509
Vps4b	Y*	0.784	0.053	1.183	0.999	1.509
Inpp4b		0.779	0.076	1.174	0.999	1.508
Oraov1	Y	0.898	0.369	1.354	0.637	1.508
Gm43660		0.916	0.76	1.382	0.419	1.508
Tcp11l2		0.711	0.019	1.072	0.999	1.508
Olfr374		0.87	0.551	1.31	0.786	1.506
Sned1	Y*	0.921	0.808	1.387	0.348	1.505

Continued on p. 1534

Table 1—Continued

Gene symbol	Predicted binding-site TargetScan	RNA fold change†	RNA *P*adj†	RIP fold change‡	RIP *P*adj†‡	RIP to RNA ratio
Gm16892		0.958	0.925	1.441	0.375	1.504
Akap2	Y	0.97	0.944	1.458	0.286	1.502
Kcnn2		0.734	0.052	1.102	0.999	1.501

Genes (n = 180) with RIP-seq to T-RNA ratio > 1.5 are shown. Y indicates the presence of at least one predicted miR-125b binding site by TargetScan mouse, version 7.2. Y* indicates target conservation in humans; †Fold change and adjusted *P* value of differential analysis of transcripts in MIN6 cells transfected with miR-125b mimics versus controls. ‡Fold change and adjusted *P* value of differential analysis of Ago2-immunoprecipitated RNAs in MIN6 cells transfected with miR-125b mimics versus controls.

in islets cultured at high glucose concentration (25 mM). To determine whether this glucose/AMPK–dependent regulation of miR-125b also occurred in vivo, we fed control, βAMPKdKO or βLKB1KO [i.e., mice with a β cell–specific deletion of the AMPK-upstream kinase liver kinase B1, and LKB1/STK11 (17)] animals a ketogenic (low-sugar) diet. As previously shown (5), βAMPKdKO islets had higher levels of miR-125b than did controls and the same was observed in βLKB1KO islets (Fig. 1*D*). Feeding a low-sugar diet resulted in a significant decrease in islet miR-125b in control animals but not in islets from βAMPKdKO and βLKB1KO mice (Fig. 1*D*). Moreover, culture of human islets with the selective AMPK activators ^{13}C and 991 (5) or with adenovirus encoding a dominant-negative form of the enzyme caused a small but significant reduction and increase, respectively, in miR-125b expression (Fig. 1*E*, Supplementary Fig. 1*E*). Taken together, these results indicate that high glucose concentration stimulates miR-125b expression in both mouse and human islets by inhibiting AMPK activity.

MiR-125b Regulates Insulin Secretion in β-Cell Lines

The most important characteristic of the β cell is its capacity to respond to high levels of circulating glucose by secreting insulin (1). Glucose-stimulated insulin secretion (GSIS) in MIN6 cells with ∼40-fold increased miR-125b (Supplementary Fig. 2*A*) after transient transfection with miR-125b mimics was lower than in control cells, and miR-125b overexpressing cells contained 25% less insulin (Fig. 1*F*, Supplementary Fig. 2*B*). Conversely, inhibition of miR-125b function with an adenovirus encoding for an miR-125b inhibitor resulted in increased GSIS and insulin content (Fig. 1*G*, Supplementary Fig. 2*C*).

To explore whether miR-125b regulated insulin secretion in a human β-cell line, we next generated human EndoCβ-H1 cells (18) with miR-125b loss of function using CRISPR-Cas9 (EndoCβ-H1-MIR125B2-KO; Fig Supplementary Fig. 3*A*). EndoCβ-H1-MIR125B2-KO cells contained ∼80% less mature miR-125b than did controls (Supplementary Fig. 3*B* and *C*), showed similar viability (Supplementary Fig. 3*D*) and, as anticipated, secreted more insulin in response to high glucose levels than did controls, although only a small, nonsignificant increase was detected in insulin content (Fig. 1*H*, Supplementary Fig. 2*D*).

A High-Throughput Approach Identifies miR-125b Target Genes

To further explore the genes and molecular pathways regulated by miR-125b, as well as its mechanism of action, we sought to explore the impact of the miRNA on β-cell gene expression and to identify direct targets in a high-throughput manner. miRNAs guide the miRISC, including an Argonaute protein, to the target mRNAs, which results in mRNA destabilization and/or inhibition of translation (19). Thus, we used an experimental approach that combined overexpression of miR-125b in MIN6 cells, immunoprecipitation of miRISC and target mRNAs using an antibody against AGO2 and high-throughput sequencing and differential analysis of cellular total and immunoprecipitated RNAs (20) (Supplementary Fig. 4*A*). As a consequence of miR-125b overexpression, we expected miR-125b targets to be reduced or unchanged (if repression occurs exclusively at the level of translation) in the T-RNA fraction (Supplementary Table 1) and increased in the RIP-RNA fraction (Supplementary Table 1). Thus, for miR-125b direct targets, we expect a RIP-RNA to T-RNA ratio >1 after miR-125b overexpression. To validate our approach we sorted all genes according to RIP-RNA to T-RNA ratio (Supplementary Table 1) and performed unbiased motifs enrichment analysis using cWords (21). As anticipated, cWords found a significant enrichment of miR-125b seed-matching sequences in both the 3′ nontranslated (3′UTR) and coding sequences (CDSs) of highly ranked (i.e., high RIP-RNA to T-RNA ratio) genes (Supplementary Fig. 4*B*), suggesting that miR-125b–mRNA target interactions occur through both these regions. A total of 180 mRNAs were enriched in miRISC after miR-125b overexpression, with an RIP-RNA to T-RNA ratio >1.5 (Fig. 2*A*, Table 1). Of these, 60 were significantly downregulated at the mRNA level after miR-125b overexpression (Table 1, adjusted *P* value [Padj] < 0.1) and 87 contained predicted binding sites in their 3′UTRs, according to TargetScan, ∼50% (n = 49) of which are conserved in humans (Table 1).

We further validated the six targets (*Taz*, *M6pr*, *Tor2a*, *Mtfp1*, *Tnks1bp1*, and *Gnpat*) with the highest RIP-RNA to T-RNA ratios using luciferase reporter–based assays (20). As expected, cotransfection of miR-125b mimics reduced

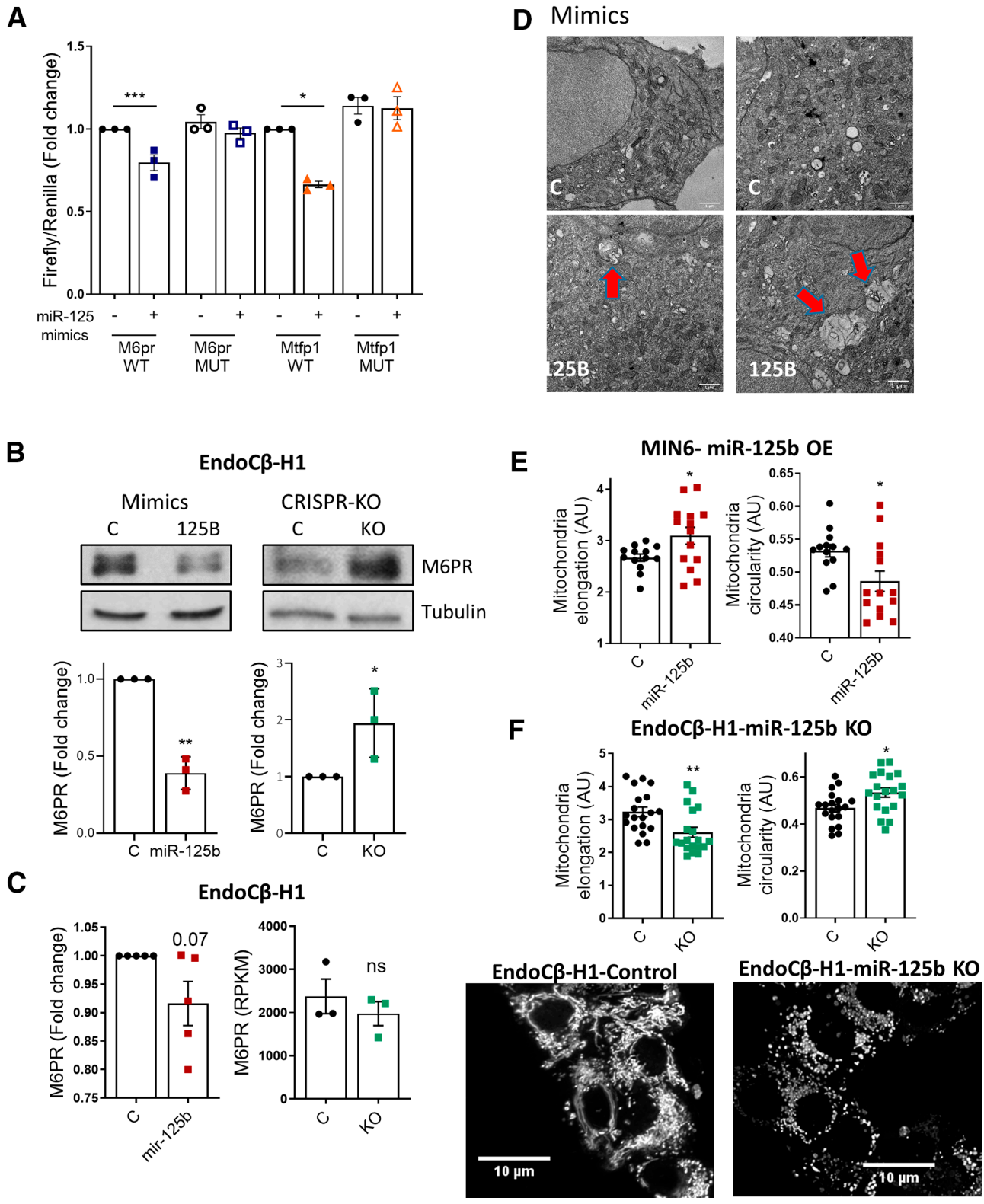

Figure 3—MiR-125b represses *M6pr* and *Mtfp1* and alters lysosomal and mitochondrial morphology. *A*: MIN6 cells were transfected with luciferase reporters containing the *M6pr* or the *Mtfp1* 3′UTRs with (mutated [MUT]) or without (wild type [WT]) two- to three-point mutations in the sequence complementary to the miR-125b seed. Control (−) or miR-125b (+) mimics were cotransfected and *Firefly* luciferase values normalized to *Renilla*. Each dot represents an independent experiment. *B*: Representative Western blot showing reduced (left panel) and increased (right panel) M6PR protein levels upon transfection with 1 nM miR-125b (miR-125b)/control (C) mimics or CRISPR-Cas9–mediated deletion of miR-125b in EndoCβ-H1 cells, respectively. Bar graphs show densitometry quantification of M6PR, using ImageJ, normalized by tubulin and presented relative to the control. *C*: Left panel: quantitative RT-PCR measurement of *M6PR* mRNA in EndoCβ-H1 cells transfected with control or miR-125b mimics, normalized by the housekeeping gene *Ppia* and presented as fold change of the control.

Firefly/Renilla activity ratios in cells transfected with constructs containing the *Taz*, *M6pr*, *Tor2a*, and *Mtfp1* 3′UTRs, *Gnpat* CDS, or three perfectly complementary sequences to miR-125b (positive control), downstream of the *Firefly* open reading frame in the bicistronic plasmid pMiRGlo, demonstrating that miR-125b silences gene expression through those sequences (Fig. 2*B*). In contrast, miR-125b mimics did not affect *Firefly/Renilla* activity of the empty vector or in the presence of the 3′UTR of *Gnpat*, which lacked predicted miR-125b binding sites. We failed to validate miR-125b action through *Tnks1bp1* CDS, perhaps because the location of the binding site downstream of the luciferase CDS and not within the CDS itself (22).

MiR-125b Targets Genes Encoding Mitochondrial and Lysosomal Proteins

To identify biological pathways and functions regulated by miR-125b, we submitted the list of genes dysregulated at the RNA level (T-RNA, n = 306 and 317 genes down- and upregulated, respectively; Padj < 0.1; Supplementary Table 1) as well as those identified as miR-125b direct targets with a RIP-RNA to T-RNA ratio > 1.5 (Table 1) to the Database for Annotation, Visualization and Integrated Discovery (23). Functional annotations with high enrichment scores included mitochondrion, tricarboxylate cycle, sterol biosynthesis, protein transport, Golgi apparatus, and endosome (Fig. 2*C*, Supplementary Table 2), all closely associated with the capacity of the β cells to produce and secrete insulin in response to glucose.

The gene at the top of our miR-125b targets list, the lysosomal- and Golgi-associated *M6pr* (manose-6-phosphate receptor–cation dependent) controls trafficking of lysosomal hydrolases from the Golgi via endosomes (24) and thus may influence protein turnover and lysosomal function. Luciferase assays further confirmed the interaction of miR-125b via a predicted, conserved miR-125b binding site in its 3′UTR (Fig. 3*A*), and Western immunoblotting of EndoCβ-H1 cells overexpressing miR-125b and EndoCβ-H1-MIR125B2-KO cells showed a strong down- and upregulation in M6PR protein, respectively (Fig. 3*B*), without significant changes at the mRNA level (Fig. 3*C*, Supplementary Table 3). These results confirm that miR-125b targets M6PR to repress protein production in human EndoCβ-H1 cells.

We hypothesized that M6PR downregulation after miR-125b overexpression may lead to a defect in lysosomal hydrolases and an accumulation of lysosomal structures with nondigested cargos. Accordingly, electron microscopy revealed an accumulation of aberrant, enlarged lysosomal structures in MIN6 cells overexpressing miR-125b (Fig. 3*D*).

Gene ontology (GO) analysis of genes dysregulated upon miR-125b overexpression also revealed a significant overrepresentation of genes involved in mitochondrial function (Supplementary Table 2, Fig. 2*C*), including one of the top miR-125b direct targets, mitochondrial fission process 1 (*Mtfp1*, also known as MTP18). Luciferase experiments further confirmed the interaction of miR-125b via a predicted conserved binding site in *Mtfp1* 3′UTR (Fig. 3*A*). MTFP1 has been implicated in mitochondrial fission and apoptosis in mammalian cells (25). To explore a possible role for miR-125b in controlling mitochondrial morphology, we stained MIN6 cells transfected with control or miR-125b mimics with a mitochondria-targeted green fluorescent probe (Mitotracker green). MIN6 cells overexpressing miR-125b contained the same number of mitochondria and overall mitochondrial area, though their mitochondria were slightly more elongated and less circular (Fig. 3*F*, Supplementary Fig. 5*A*). In contrast, EndoCβ-H1-*MIR125B2-KO* cells revealed a marked reduction in mitochondrial area and the number of mitochondria with a smaller perimeter, which were also less elongated and more circular (Fig. 3*F*, Supplementary Fig. 5*B*). Further emphasizing the importance of miR-125b for mitochondrial homeostasis, GO analysis following RNA sequencing (RNA-seq) of EndoCβ-H1-MIR125B2-KO confirmed a strong enrichment in dysregulated genes associated with mitochondrial function (Supplementary Fig. 5*C*, Supplementary Table 4), including *MTFP1* (1.5-fold, P = 0.006, Padj < 0.1). These findings suggest that relief from miR125-mediated repression leads to disruption of the tubule-vesicular network and to profound changes in the expression of genes involved in mitochondrial homeostasis, which may underlie the observed improvement in insulin secretion.

MiR-125b Overexpression in β Cells Impairs Glucose Tolerance In Vivo

Given the regulatory effect of miR-125b in vitro, we decided to study the role of miR-125b in vivo by generating a mouse with β cell–specific, doxycycline-inducible overexpression of miR-125b using a RIP7-rtTA promoter (14). MIR125B-Tg (MIR125B-Tg: RIP7-rtTA$^{+/-}$, MIR125B Tg$^{+/-}$) animals contained ∼60-fold more islet miR-125b than did controls

Right panel: Normalized (reads per kilobase of transcript per million mapped reads) M6PR reads in control versus MIR125B2-KO (KO) EndoCβ-H1 cells. *D*: Representative TEM image of MIN6 cells transfected for 48 h with control or miR-125b (125B) mimics. Red arrows point to enlarged lysosomal structures. Scale bar = 1 μm. These were not observed in any of the imaged controls (n = 3 independent experiments). *E* and *F*: Quantitative analysis of mitochondria number and morphology on deconvoluted confocal images of (*E*) MIN6 cells transfected with miR-125b (red) or control (black) mimics or (*F*) EndoCβ-H1 with CRISPR/Cas9–mediated miR-125b deletion (green) or controls (black). Cells were stained with Mitotracker green. An ImageJ macro was generated and used to quantify individual mitochondria length (elongation) and circularity (0: elongated; 1: circular). Each dot represents one acquisition [n = 3 (*E*), n = 4 (*F*) independent experiments]. Lower panels show representative confocal images of the mitochondrial network of EndoCβ-H1-MIR125B2-KO and control cells. Scale bar: 10 μm. Error bars represent SEM. *P < 0.05, **P < 0.01, ***P < 0.001, paired Student t test of the log(fold change) values (*A–C*); Welch t test (*E* and *F*). a.u., arbitrary units; OE, overexpression.

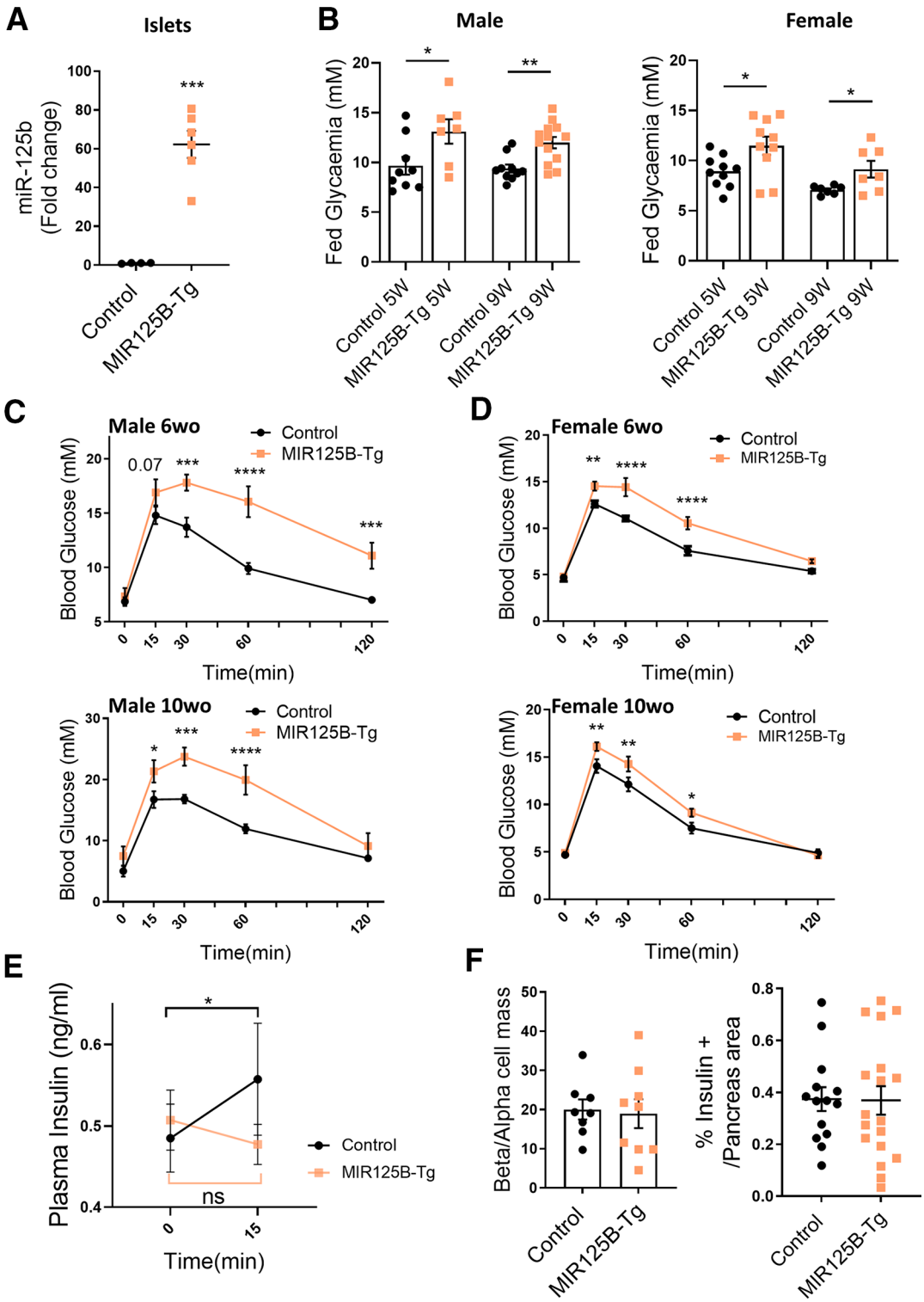

Figure 4—Mice with β cell–selective overexpression of miR-125b are glucose intolerant and have impaired glucose stimulated insulin secretion. *A*: MiR-125b quantitative RT-PCR in isolated islets from control (RIP7-rtTA$^{+/-}$) and MIR125B-Tg mice (RIP7-rtTA$^{+/-}$, MIR125B Tg$^{+/-}$). Data are fold change versus control. *B*: Glycemia in 5- and 9-week-old control and MiR125B-Tg mice fed ad libitum. *A* and *B*: Each dot represents a single mouse. *C* and *D*: Glucose tolerance test in 6- and 10-week-old MIR125B-Tg and littermate control male (*C*) and female (*D*) mice (n = 7–8 control mice; n = 5–7 MiR125B-Tg mice). *E*: Insulin secretion, induced by 3 g/kg glucose, was assessed in 10-week-old MIR125B-Tg and littermate controls (n = 13 control mice; n = 11 MiR125B-Tg mice). *F*: Pancreata from MIR125B-Tg and littermate controls were fixed and subjected to immunocytochemical analysis for insulin and glucagon. β- and α-cell masses are presented as the β-cell to α-cell ratio and correspond to quantification of insulin-positive area to glucagon-positive area ratio (left panel). β-Cell mass is presented as a percentage of the pancreatic surface and corresponds to quantification of the insulin-positive area per pancreas area quantified in whole pancreas sections. Each dot represents one pancreatic section (n = 3 mice/genotype). Error bars represent SEM. *$P < 0.05$, **$P < 0.01$, ***$P < 0.001$, ****$P < 0.0001$, Welch test (*A*, *B*, *F*); two-way ANOVA (repeated-measures), Fisher least significance different test (*C*–*E*).

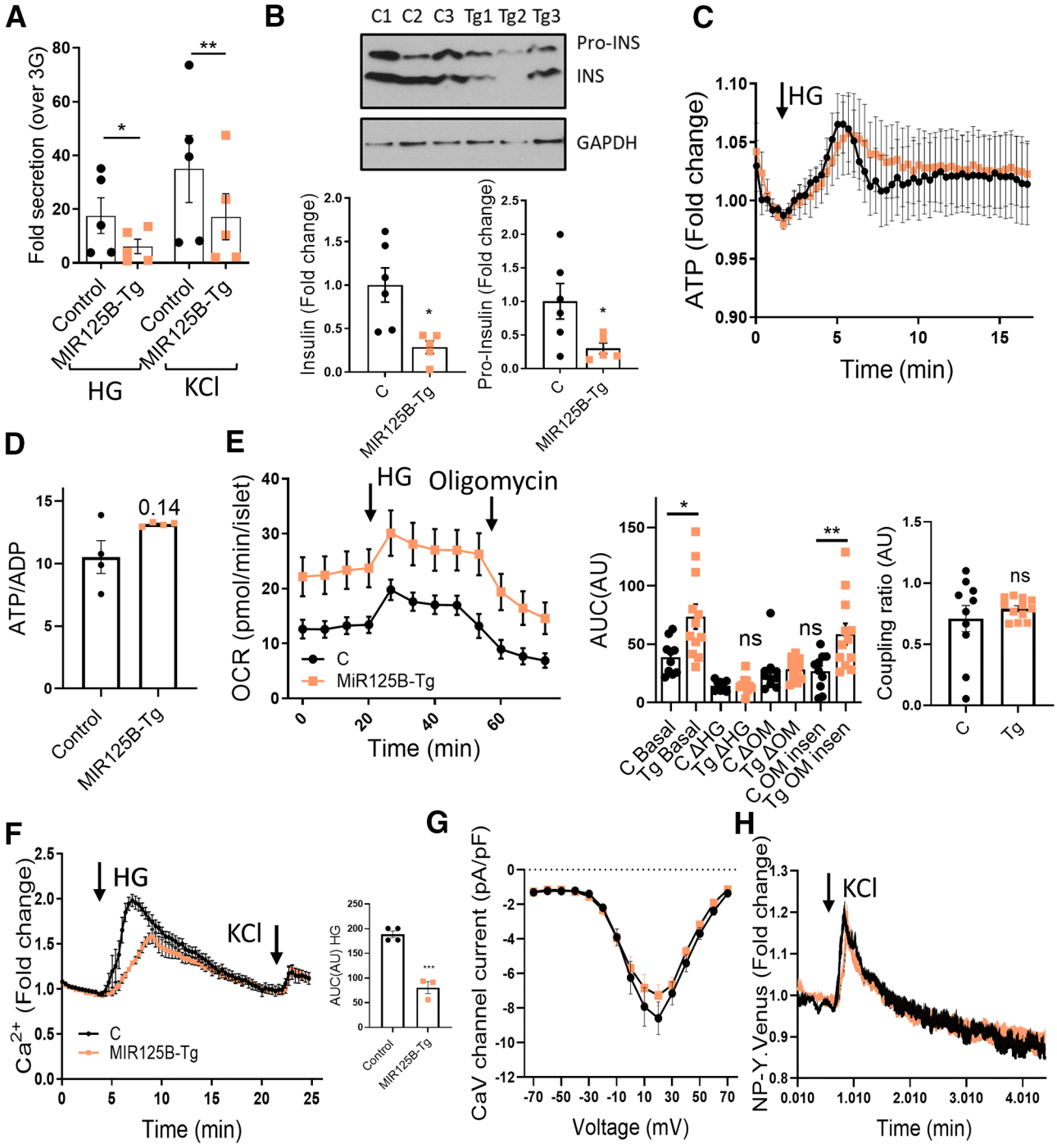

Figure 5—MIR125B-Tg islets contain and secrete less insulin than do control islets. *A*: Fold induction insulin secretion versus low glucose (3 mM; LG) in response to 30-min high glucose (HG; 17mM) or KCl (17mM KCl and 3 mM glucose) in islets from 10- to 11-week-old control (RIP7-rtTA$^{+/-}$) and MIR125B-Tg (RIP7-rtTA$^{+/-}$, MIR125B Tg$^{+/-}$) mice. *B*: Insulin (INS) and proinsulin (Pro-INS) content in 10-week-old control (C) and MIR125B-Tg (Tg) mice. A representative Western blot is shown with islets from three control and three MIR125B-Tg animals. Bar graphs show densitometry quantification of insulin and proinsulin, using ImageJ, normalized by GAPDH and presented relative to the average control. *C* and *D*: ATP levels increase in response to high glucose (17 mM vs. 3 mM) (*C*) and ATP to ADP ratio at 3 mM glucose in intact MIR125B-Tg and control islets infected with an adenoviral Perceval sensor (*D*). n = 4–5 mice/genotype, with 1–2 acquisitions per mouse and an average of five islets/acquisition. *E*: Oxygen consumption rate (OCR) measured in the presence of 3 mM or 17 mM (HG) glucose and 5 μM oligomycin (OM) over time, as indicated. Islets were preincubated for 1 h at 3 mM glucose. Left panel shows traces from the actual experiment. Middle and right panels show calculations during the indicated periods. "Basal" shows the area under the curve (AUC) under basal (3 mM) conditions; ΔHG and −ΔOM report the change in respiration when 17 mM glucose and oligomycin are added, respectively. The oligomycin insensitive value (OM insen) reports the residual respiration after the addition of oligomycin and coupling ratio (right panel) represents the oligomycin-sensitive respiration divided by respiration preceding oligomycin. Each dot represents a plate well with three to six size-matched islets (n = 10–12) extracted from three control (C) and four MIR125B-Tg (Tg) mice. *F*: Ca^{2+}

(RIP7-rtTA$^{+/-}$) (Fig. 4*A*), whereas statistically significant changes were not detected in miR-125b levels in the hypothalamus, a potential site for activity of the RIP promoter (26) (Supplementary Fig. 6*A*).

MIR125B-Tg mice had indistinguishable weight gain compared with control mice (Supplementary Fig. 6*B*), whereas random-fed glycemia incidence was significantly higher in both male and female MIR-125B-Tg mice (Fig. 4*B*). Consistently, MIR125B-Tg mice were highly glucose intolerant (Fig. 4*C* and *D*), though fasting glycemia was unaffected. No changes in glucose tolerance were observed in animals bearing the transgene in the absence of rtTA (-rtTA control: RIP7-rtTA$^{-/-}$, MIR125B OE$^{+/-}$; Supplementary Fig. 6*C*), demonstrating that the defects observed were not due to an off-target genomic event resulting from transgene integration. Blood glucose levels were efficiently reduced by administration of exogenous insulin, excluding insulin insensitivity as a major player in the glucose intolerance observed in MIR125B-Tg animals (Supplementary Fig. 6*D*). Moreover, plasma insulin did not increase in MIR125B-Tg mice in response to an intraperitoneal injection of glucose (Fig. 4*E*), suggesting impaired β-cell secretory function. β-cell mass and β- to α-cell ratio, as well as proliferation and apoptosis, remained unchanged in the transgenic animals (Fig. 4*F*, Supplementary Fig. 6*E* and *F*). Taken together, these data suggest that increased miR-125b in the β-cell results in hyperglycemia and glucose intolerance due to impaired β-cell secretory function.

MiR-125b Transgenic Islets Contain and Secrete Less Insulin

To further explore a cell autonomous defect in insulin secretion, we measured GSIS in isolated islets from MIR125B-Tg mice, which showed a strong reduction in insulin secretion in response to glucose or depolarization by KCl (Fig. 5*A*, Supplementary Fig. 6*G*). Consistent with our previous data from MIN6 cells, MIR125B-Tg islets contained less intracellular insulin (Supplementary Fig. 6*H*), as further confirmed by Western blot (Fig. 5*B*, Supplementary Fig. 6*I*), revealing lower levels of both intracellular proinsulin and insulin. Accordingly, MiR125B-Tg pancreata contained less insulin (Supplementary Fig. 6*J*). These data indicate a reduced capacity of MIR125B-Tg β cells to produce and secrete insulin.

Upon entry in the β cell, glucose is rapidly metabolized by mitochondria, causing a sharp increase in intracellular ATP to ADP ratio, closure of ATP-sensitive K^+ channels, plasma membrane depolarization, and Ca^{2+} influx into the cytosol to trigger insulin exocytosis (1). That secretory responses to both high glucose and KCl levels were impaired in MIR125B-Tg islets suggested defects downstream of glucose metabolism. Accordingly, the glucose-mediated ATP to ADP ratio increase and the basal ATP to ADP ratio were similar in MIR125B-Tg and control isolated islets (Fig. 5*C* and *D*). Oxygen consumption rate increases induced by high glucose levels and in response to the inhibitor of mitochondrial ATP synthase oligomycin were also comparable (Fig. 5*E*), confirming similar mitochondrial capacity to generate ATP. In contrast, both basal and oligomycin-insensitive respiration were significantly elevated in MIR125B-Tg islets (Fig. 5*E*), suggesting increased inner mitochondrial membrane proton conductance. Additionally, MIR125B-Tg islets had a strong reduction in glucose-induced changes in intracellular Ca^{2+} (Fig. 5*F*). KCl-induced increases in Ca^{2+} were similar between MIR-125B-Tg and control islets (Fig. 5*F*), suggesting that MIR125B-Tg β cells contained functional voltage-gated calcium channels. This was further confirmed in single β cells by whole-cell voltage clamp that showed similar VDCC currents (Fig. 5*G*). The kinetics of individual fusion events were also identical in cells from MIR125B-Tg or control islets (Fig. 5*H*), as assessed by total internal reflection of fluorescence imaging of neuropeptide Y (NPY)-Venus–expressing vesicles near the plasma membrane (27), indicating that vesicle fusion itself was not affected by miR-125b overexpression.

Enlarged Lysosomes and Autophagolysosomes Are Abundant in miR-125b Transgenic Islets

Our previous experiments in cell lines pointed to miR-125b as a regulator of mitochondrial and lysosomal function, which could contribute to defective insulin secretion. In contrast to our observations in cell lines, but consistent with an efficient capacity to generate ATP in response to glucose, mitochondrial area and morphology and the levels of mitochondrial DNA (Fig. 6*B*) were comparable in MIR125B-Tg and control islets (Fig. 6*A* and *B*). Even though lysotracker staining revealed no differences in lysosomal area or numbers (Supplementary Fig. 6*K*), transmission electron microscopy (TEM) identified the presence of enlarged lysosomes and autophagosomes in the MIR125B-Tg islets, which were rarely found in control samples (Fig. 6*C* and *D*). Moreover, islet coimmunostaining identified a significant reduction in the lysosomal protease cathepsin D localized to (LAMP1-positive) lysosomes (Fig. 6*F*). TEM also revealed a sharp

concentration increases in response to high glucose (17 mM vs. 3 mM) and KCl (20 mM KCl, 3 mM glucose) in intact MIR125B-Tg and control islets incubated with Cal-520. n = 4–5 mice/genotype, with one to two acquisitions per mouse and an average of five islets/acquisition. AUC corresponding to HG incubation was determined and is presented in the bar chart. *G*: Average maximum voltage-dependent Ca^{2+} current densities recorded from control and MIR125B-Tg β cells in response to 10 mV steps from −70 to 70 mV. *n* = 16 and 29 β cells from two control and four MIR125B-Tg mice. *H*: NPY-Venus fluorescence increases in response to 20 mM KCl in cells from dissociated MIR125B-Tg and control islets infected with an adenoviral NPY-Venus sensor. *n* = 3–4 control mice/genotype with two acquisitions per mouse and one to two β cells per acquisition. Each dot represents a single mouse in all graphs unless otherwise indicated. Error bars represent SEM. $*P < 0.05$, $**P < 0.01$, $***P < 0.001$, two-way ANOVA (repeated-measures) and Bonferroni multiple comparisons test (*A*), paired Student (*B*) and unpaired Welch (*D* and *E*) or Student *t* test (*F*). Δ, change in; a.u., arbitrary units; ns, not significant.

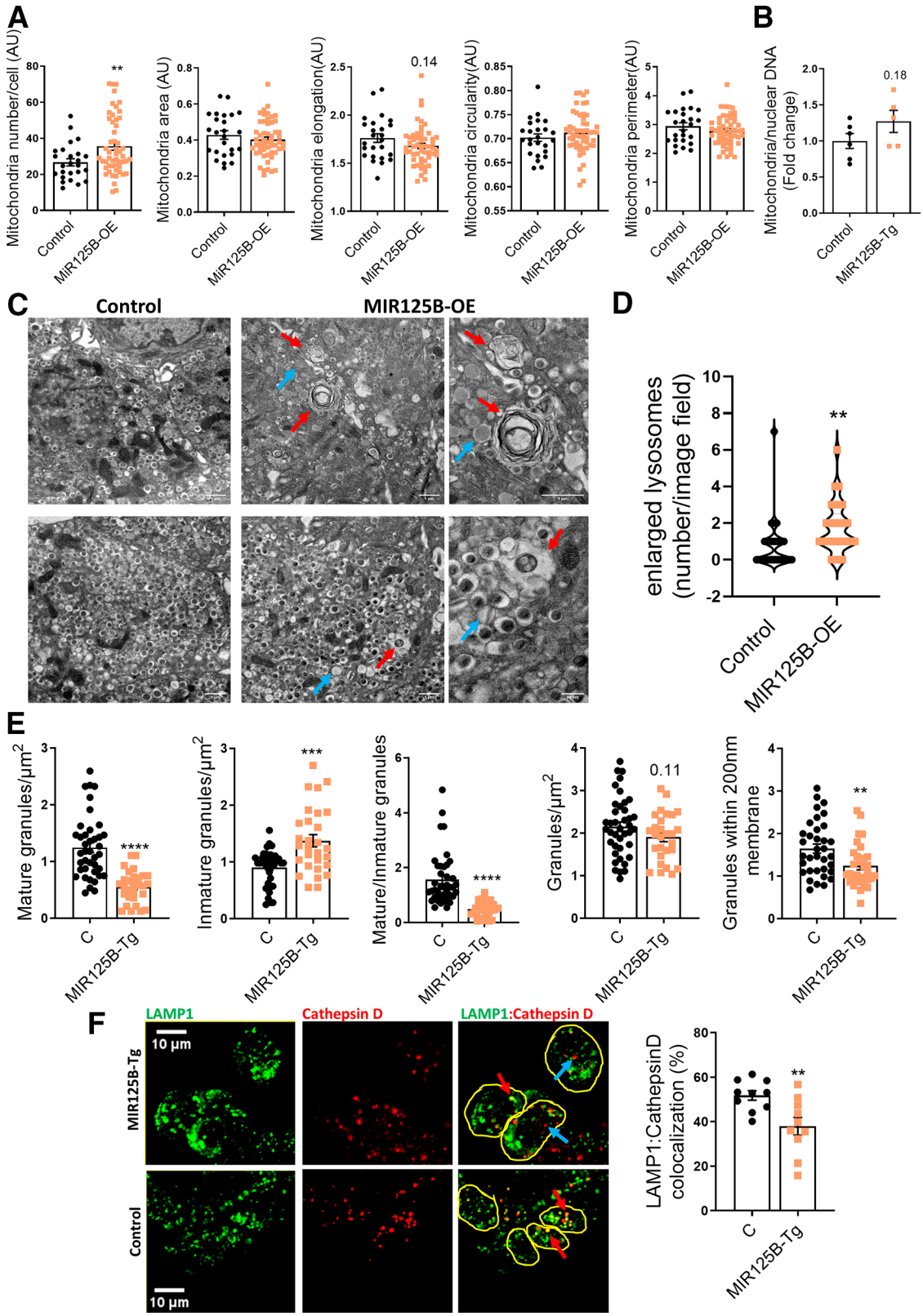

Figure 6—Enlarged lysosomes and autophagolysosomes are abundant in miR-125b transgenic islets. *A*: Quantitative analysis of mitochondria number and morphology on deconvoluted confocal images of dissociated MIR125B-Tg and control islets from 10- to 11-week-old mice. Cells were stained with Mitotracker green. An ImageJ macro was generated and used to quantify the number of mitochondria per cell, total mitochondria area, individual mitochondria length (elongation), circularity (0: elongated; 1: circular), and perimeter. Each dot represents one cell (n = 3 mice/genotype). *B*: Mitochondrial DNA copy number, calculated as the ratio of the mitochondrial encoded gene mt-Nd1 to the nuclear Cxcl12. Each dot represents a single mouse. *C*: Representative TEM images of MIR125B-Tg and control β cells.

reduction in the number of dense-core insulin granules and an increase in granules with defective crystallization (light–core, abnormal rod-like, or empty) (Fig. 6*C* and *E*). Importantly, fewer secretory granules were present within 200 nm of the plasma membrane in MIR125B-Tg than in control islets (Fig. 6*E*).

β-Cell Identity Is Altered in MIR125b-Tg Islets

To shed more light on the molecular mechanisms underlying the secretory defects of miR-125B-Tg islets, we performed RNA-seq on MIR125B-Tg and control islets. We found 320 and 398 genes were significantly (*P*adj < 0.1) down- and upregulated, respectively (Supplementary Table 5).

GO analysis of downregulated genes identified a strong enrichment within pathways and processes associated with mature β-cell function, such as regulation of insulin secretion and endocrine pancreas development (Supplementary Table 6, Fig. 7*A* and *B*, Supplementary Fig. 7*A*), with a significant reduction of several important β-cell identity genes, such as *Ucn3, Pdx1, NeuroD1, Nkx2.2, Slc2a2*, and *Nkx6.1*. These genes either do not contain predicted miR-125b binding sites or had been identified as direct miR-125b targets in our RNA-immunoprecipitation sequencing (RIP-seq) experiments, suggesting an indirect effect. Further supporting a loss of β-cell identity, upregulated genes were significantly associated with neuronal features (Supplementary Table 6, Fig. 7*A*, Supplementary Fig. 7*B*). We also observed an upregulation of many glycoprotein genes and of genes associated with cellular and focal adhesion, signaling pathways and voltage-gated and potassium channels. Golgi-associated genes were both up- and downregulated (Supplementary Table 6, Fig. 7*A*, Supplementary Fig. 7*B*).

MiR-125b Alters Insulin Secretion and Gene Expression in Human Islets

To further explore the relevance of miR-125b in human β cells, we performed GSIS assays in human islets infected with Ad-MIR125B, achieving a ∼4.5-fold increase in miR-125b levels (Supplementary Fig. 8*A*). MiR-125b–overexpressing islets secreted ∼50% less insulin than did controls, though their insulin content remained unchanged (Fig. 7*C*, Supplementary Fig. 8*B*). Additionally, we performed RNA-seq in dissociated human islets infected with these viruses, achieving an approximately threefold increase in miR-125b (Supplementary Fig. 8*C*). Principal component analysis showed that most of the variation was due to the donor origin of the islets (Supplementary Fig. 8*D*); thus, this experiment was underpowered (∼20% to detect a twofold change, with $P < 0.01$, calculated using the Scotty web tool (28)). Nevertheless, the expression of hundreds of genes tended to be altered ($P < 0.05$; Supplementary Table 7) and gene set enrichment analysis of all the genes ranked by gene expression fold change identified a significant enrichment in several biological pathways (Supplementary Fig. 8*E* and *F*, Supplementary Table 8) notably including lysosomal ($P < 0.0001$; false discovery rate = 0.07) and calcium signaling ($P < 0.0001$; false discovery rate = 0.06). Further suggesting a role for miR-125b in lysosomal function, a downregulation in M6PR protein was observed in dissociated human islets infected with Ad-MIR125B (Fig. 7*D*).

DISCUSSION

Even though elevated levels of circulating miR-125b in association with higher HbA_{1c} in type 1 diabetes (29) and T2D (30) have been previously identified, this is the first study, to our knowledge, to demonstrate that miR-125b expression is induced by glucose in mouse and human islets in an AMPK-dependent manner. Although our capacity to demonstrate a correlation between hyperglycemia and islet miR-125b levels in human islets in vivo was limited by the lack of HbA_{1c} data, we found a significantly positive correlation with donor BMI, which often is associated with HbA_{1c} (31).

Despite being highly expressed in β cells, the function and mechanism of action of miR-125b in these cells have remained elusive until now. Here, we show that elevated expression of this miRNA in β cells impairs their secretory function in vitro and in vivo.

We have generated a transgenic model capable of β-cell selective overexpression of miR-125b. These animals were hyperglycemic and strongly glucose intolerant and presented a drastic reduction in circulating insulin after a glucose challenge.

Our findings suggest two main causes for the secretory defects in the MIR125b-Tg mice: strong impairment in GSIS and reduced insulin content. Unlike ATP, levels of cytosolic Ca^{2+} increased after glucose stimulation were substantially lower in MIR125b-Tg islets, though, paradoxically, similar levels of Ca^{2+} were observed upon membrane depolarization with KCl, even though KCl-stimulated insulin secretion was also strongly impaired. This points toward defects at different levels on the secretory pathway, as supported by the striking changes in gene expression. First, ATP-sensitive

Red arrows: enlarged lysosomes with undigested cargos. Blue arrows: noncrystalized insulin granules, showing a rod-like structure or a gray interior. Scale bar = 1 μm, except 40 nm in right-hand side panels. *D*: Number of enlarged lysosomes per field imaged. *E*: β-cell granule density. *D* and *E*: Each dot represents one image (n = 3 mice/genotype, 9–13 images/mouse). *F*: Representative confocal microscopy images of β cells within MIR125B-Tg and control islets immunostained with anti-cathepsin D (red) and anti-LAMP1 (green) antibodies. Yellow circles represent individual cells. Blue arrows show examples of only cathepsin-positive particles and red arrows show particles positive for both LAMP1 and cathepsin D staining. ImageJ was used to quantify cathepsin D and LAMP1–stained particles within each cell, represented in the accompanying bar chart as a percentage of LAMP1-positive particles per cell. Each dot represents an individual islet with an average of three to eight cells quantified per islet, extracted from two control (C) and two MIR125B-Tg mice. Error bars represent SEM. *$P < 0.05$, **$P < 0.01$, ****$P < 0.0001$, Welch *t* test.

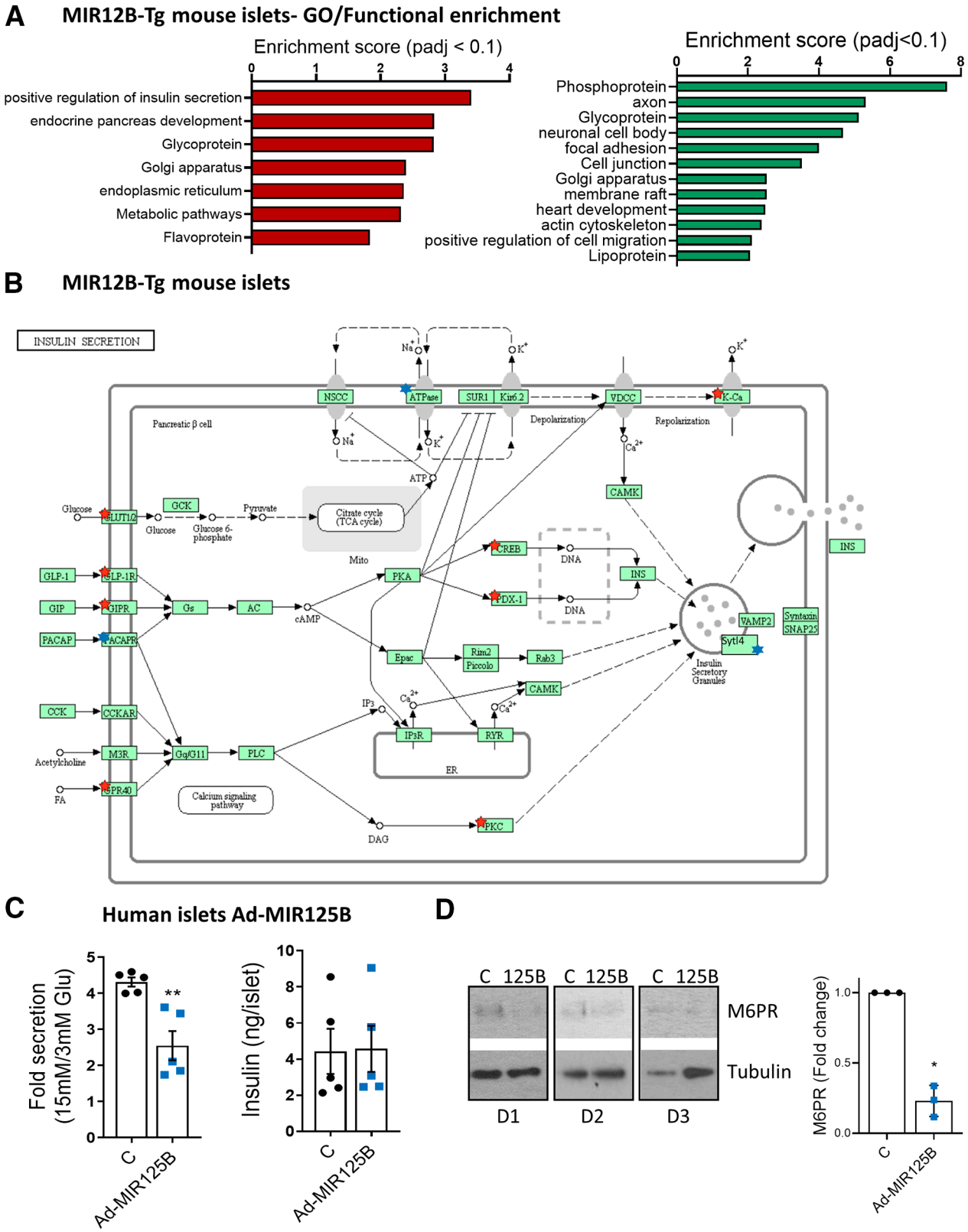

Figure 7—MiR125b overexpression alters gene expression in mouse and human islets. *A*: GO analysis of significantly (*P*adj < 0.1) down-regulated (left, red) and upregulated genes (right, green) in MIR125B-Tg islets from 6-week-old mice versus control mice, performed with the Database for Annotation, Visualization and Integrated Discovery. The graph shows enrichment scores for one representative term for each cluster grouped by semantic similarities and including terms with *P*adj (Benjamini) < 0.05. See Supplementary Table 6 for a full list of terms. *B*: Kyoto Encyclopedia of Genes and Genomes pathway "Insulin secretion." Red and blue stars indicate significantly down- and up-regulated genes in MIR125B-Tg islets versus control islets, respectively. *Sytl4* (granuphilin) has been manually added to the pathway.

K^+–independent amplification pathways (32) might be impaired in MIR125B-Tg islets, which display lower levels of genes encoding enzymes limiting the production of guanine nucleotides and glutamine, such as *Imphd1* and *GLUL*, that can promote insulin exocytosis in an ATP- and ADP-independent manner (33, 34). Second, voltage-clamp electrophysiology experiments confirmed the presence of functional VDCC in MIR125B-Tg β cells. MIR125B-Tg islets expressed normal levels of Ca^{2+} channels but higher levels of PMCA3 and the Na^+/Ca^{2+}-exchanger NCX3, members of protein families responsible for Ca^{2+} extrusion in β cells, which could potentially contribute to reduced levels of cytosolic calcium. Third, TEM revealed fewer granules in close proximity to the plasma membrane in MIR125B-Tg β cells, and RNA-seq identified a strong alteration in genes involved in cellular granule docking and fusion, such as granuphilin (*Sytl4*), the SNARE protein *Vamp3*, and synaptotagmins (*Syt1*, *Syt12*, and *Syt17*) (35, 36), pointing toward defects in the final steps of exocytosis. Finally, MIR125B-Tg islets present defective granule crystallization, which might be partially due to reduced levels of the zinc transporter *Znt8* mRNA (37). Loss of β-cell identity might further contribute to these secretory defects, though some of these transcriptional changes may occur as a consequence of the moderate fed hyperglycemia in these animals (38) or be residual from impaired maturation, because RIP7-rtTA–driven transgene expression is expected to occur in 11.5-day-old transgenic embryos.

Here, we unbiasedly identified dozens of miR-125b targets through the integration of RIP-seq and RNA-seq data (8,20) of miR-125b–overexpressing MIN6 cells. Given the supraphysiological levels of miR-125b achieved in these experiments, additional loss-of-function experiments will be key to confirm the targeting. It remains to be studied whether some of these targets are shared with the family member miR-125a, also expressed in β cells. Additionally, some of these targets might not be conserved in humans, and this may explain the fact that miR-125b modulation affects insulin content in mouse β cells but less so in humans. Intriguingly, disheveled binding antagonist of β catenin 1 (*Dact1*) was not in this list and remained unchanged upon miR-125 manipulation in all our experimental models. *Dact1* was previously identified as an miR-125b target in β cells, perhaps because of the presence of other pancreatic, highly proliferative cells in the samples (39).

One of the genes at the top of our list of miR-125b targets, *M6pr,* encodes the cation-dependent manose-6-phosphate protein MP6R (CD-M6PR). Even though the function of CD-M6PR remains unknown in β cells, this receptor is necessary for adequate lysosomal targeting of several hydrolases, such as cathepsin D (40). Remarkably, MIR125B-Tg islets contained less cathepsin D in their lysosomes, which appeared enlarged similarly to those observed by Masini et al. (41) in T2D islet micrographs, suggesting the accumulation of undigested cargos. Defects on the lysosomal or trafficking machinery can also affect the maturation, packaging, and location of the secretory granules within the cell (42) and might contribute to the reduced insulin content and crystallization defects observed in the MIR125B-Tg mice. Whether, and how, elevated miR-125b during hyperglycemia or loss of AMPK activity contributes to these processes in T2D remains to be studied.

Even though we had identified several genes encoding mitochondrial proteins as miR-125b targets in MIN6 cells, no mitochondrial morphological defects were detected in the transgenic islets, suggesting that endogenous miR125b levels are sufficient to exert maximal effects on mitochondrial structure. However, several mitochondrial genes were dysregulated in MIR125B-Tg islets and seahorse experiments showed a significant increase in basal and oligomycin-insensitive respiration, suggesting a certain extent of mitochondrial dysfunction.

On the other hand, deletion of miR-125b in EndoCβ-H1 cells resulted in a strong alteration of mitochondrial morphology and in the expression of mitochondrial proteins, including the miR-125b targets *Mtfp1* and *Gnpat*. *Mtfp1* is targeted by miR-125b in monocytes to promote elongation of the mitochondrial network (43). GNPAT stabilizes DRP1 (44), which is required for mitochondrial fission and deletion of which impaired insulin secretion (45, 46). In line with these earlier studies, EndoCβ-H1-MIR125B2-KO cells contained shorter mitochondria, which correlated with increased GSIS. It has been contested, however, whether mitochondrial fragmentation promotes apoptosis or correlates with hyperglycemia or diabetes (15, 47). Importantly, we did not observe any differences in cellular death or number in EndoCβ-H1-MIR125B2-KO or in *Ddit3* (CHOP) mRNA levels, suggesting an absence of mitochondrial-induced endoplasmic reticulum stress in these cells. Experiments are required to determine whether the positive effects of miR-125b elimination in β-cell function persist under conditions of cellular stress.

In summary, our results suggest that β-cell miR-125b has the potential to act as a glucose-regulated metabolic switch between the lysosomal system and mitochondria dynamics. Whole-body *MIR125B-2* knockout mice eating a high-fat diet develop insulin resistance and glucose intolerance, possibly because of the white fat accumulation (48). Nevertheless, insulin secretion or an effect in other metabolic organs were not assessed and our study provides compelling evidence of a role for miR-125b in controlling

C: GSIS (left panel) and insulin content (right panel) quantified after 30 min of 15 mmol/L glucose stimulation after 1 h preincubation at 3 mmol/L glucose of human islets infected with adenovirus expressing miR-125b (Ad-MIR125B) or a nontargeting control (C) at a multiplicity of infection (MOI) of 5 MOI 48 h before the experiments. GSIS data are presented as fold change of basal level. Each dot represents an independent experiment performed with islets from two different donors. *D*: Western blot showing reduced M6PR protein-level infection of dissociated human islets from three different donors (D1, D2, D3) infected with Ad-MIR125B or control adenovirus (MOI = 2) for 48 h. Bar graphs show densitometry quantification of M6PR, using ImageJ, normalized by tubulin and presented relative to the control.

insulin secretion and strongly indicates that nontargeted administration of miR-125b mimics may reach the islet and lead to defective β-cell function and worsen diabetes.

Studies focused on β cell–specific inhibition of miR-125b and on the function of specific targets will be essential to confirm a potential therapeutic benefit of targeting this miRNA or its targets for the treatment of diabetes.

Acknowledgments. The authors thank Stephen M. Rothery from the Facility for Imaging by Light Microscopy at Imperial College London for support with confocal and widefield microscopy image acquisition and analysis.

Funding. A.M.-S. was supported by an MRC New Investigator Research Grant (MR/P023223/1). G.A.R. was supported by a Wellcome Trust Senior Investigator Award (WT098424AIA) and Investigator Award (212625/Z/18/Z) and MRC Programme grants (MR/R022259/1, MR/J0003042/1, MR/L020149/1). A.To. was funded by the MRC (MR/R010676/1). I.L. was supported by a Diabetes UK project grant (16/0005485). This project has received funding from the European Union's Horizon 2020 research and innovation program via the Innovative Medicines Initiative 2 Joint Undertaking under grant agreement 115881 (RHAPSODY) to G.A.R. and P.M. Human islet preparations (Milan, Italy) were obtained from the European Consortium for Islet Transplantation; the Human Islet Distribution program was supported by Juvenile Diabetes Research Foundation Grant 3-RSC-2016-160-I-X.

Duality of Interest. No potential conflicts of interest relevant to this article were reported.

Author Contributions. R.C. and G.P. performed most experiments, designed research studies, and obtained and analyzed data. P.C. performed research studies (total internal reflection of fluorescence) and designed microscopy macros. D.R. assisted with computational analysis of RNA-sequencing and RNA-immunoprecipitation sequencing data. A.To. and T.B. performed transmission electron microscopy experiments. Z.W., A.S., A.Th., A.M., and Y.C. performed research studies (insulin secretion, β-cell mass and apoptosis, and Western blot, respectively). M.-S.N.-T. assisted with animal studies (in vivo insulin secretion). M.T.D. and D.A.J. performed whole-cell voltage clamp experiments. P.M., K.B., J.S., L.P., and E.d.K. provided human islets. I.L. assisted with maintenance of animal colonies. K.S. and D.M.S. provided C13 and C991, respectively. G.A.R. contributed to the study design, with reagents and AMPK and LKB1 KO animals, and in writing the manuscript. A.M.-S. conceived the study, designed and performed experiments, analyzed data, and wrote the manuscript. All authors read and approved the manuscript. A.M.-S. is the guarantor of this work and, as such, had full access to all the data in the study and takes responsibility for the integrity of the data and the accuracy of the data analysis.

Prior Presentation. Parts of this study were presented at the 79th Scientific Sessions of the American Diabetes Association, San Francisco, CA, 7–11 June 2019.

References

1. Rutter GA, Pullen TJ, Hodson DJ, Martinez-Sanchez A. Pancreatic beta cell identity, glucose sensing and the control of insulin secretion. Biochem J 2015;466:202–218

2. Swisa A, Glaser B, Dor Y. Metabolic stress and compromised identity of pancreatic beta cells. Front Genet 2017;8:21

3. Martinez-Sanchez A, Rutter GA, Latreille M. MiRNAs in β-cell development, identity, and disease. Front Genet 2016;7:226

4. Sun YM, Lin KY, Chen YQ. Diverse functions of miR-125 family in different cell contexts. J Hematol Oncol 2013;6:6

5. Martinez-Sanchez A, Nguyen-Tu MS, Cebola I, et al. MiR-184 expression is regulated by AMPK in pancreatic islets. FASEB J 2018;32:2587–2600

6. Jaafar R, Tran S, Shah AN, et al. mTORC1 to AMPK switching underlies β-cell metabolic plasticity during maturation and diabetes. J Clin Invest 2019;129:4124–4137

7. Ravassard P, Hazhouz Y, Pechberty S, et al. A genetically engineered human pancreatic β cell line exhibiting glucose-inducible insulin secretion. J Clin Invest 2011;121:3589–3597

8. Ottaviani S, Stebbing J, Frampton AE, et al. TGF-β induces miR-100 and miR-125b but blocks let-7a through LIN28B controlling PDAC progression. Nat Commun 2018;9:1845

9. Patro R, Duggal G, Love MI, Irizarry RA, Kingsford C. Salmon provides fast and bias-aware quantification of transcript expression. Nat Methods 2017;14:417–419

10. Love MI, Huber W, Anders S. Moderated estimation of fold change and dispersion for RNA-seq data with DESeq2. Genome Biol 2014;15:550

11. Martinez-Sanchez A, Nguyen-Tu MS, Rutter GA. DICER inactivation identifies pancreatic beta-cell "disallowed" genes targeted by microRNAs. Mol Endocrinol 2015;29:1067–1079

12. Jones B, Buenaventura T, Kanda N, et al. Targeting GLP-1 receptor trafficking to improve agonist efficacy. Nat Commun 2018;9:1602

13. Pasquier A, Vivot K, Erbs E, et al. Lysosomal degradation of newly formed insulin granules contributes to β cell failure in diabetes. Nat Commun 2019; 10:3312

14. Martinez-Sanchez A, Pullen TJ, Chabosseau P, et al. Disallowance of Acot7 in beta-cells is required for normal glucose tolerance and insulin secretion. Diabetes 2016;65:1268–1282

15. Georgiadou E, Muralidharan C, Martinez M, et al. Pancreatic beta cell selective deletion of mitofusins 1 and 2 (*Mfn1* and *Mfn2*) disrupts mitochondrial architecture and abrogates glucose-stimulated insulin secretion *in vivo*. 24 April 2020 [preprint] bioRxiv https://doi.org/10.1101/2020.04.22.055384

16. Kim S. ppcor: an R package for a fast calculation to semi-partial correlation coefficients. Commun Stat Appl Methods 2015;22:665–674

17. Kone M, Pullen TJ, Sun G, et al. LKB1 and AMPK differentially regulate pancreatic beta-cell identity. FASEB J 2014;28:4972–4985

18. Scharfmann R, Pechberty S, Hazhouz Y, et al. Development of a conditionally immortalized human pancreatic β cell line. J Clin Invest 2014;124:2087–2098

19. Bartel DP. MicroRNAs: target recognition and regulatory functions. Cell 2009;136:215–233

20. Martinez-Sanchez A, Lazzarano S, Sharma E, Lockstone H, Murphy CL. High-throughput identification of MiR-145 targets in human articular chondrocytes. Life (Basel) 2020;10:58

21. Rasmussen SH, Jacobsen A, Krogh A. cWords - systematic microRNA regulatory motif discovery from mRNA expression data. Silence 2013;4:2

22. Zhang K, Zhang X, Cai Z, et al. A novel class of microRNA-recognition elements that function only within open reading frames. Nat Struct Mol Biol 2018;25:1019–1027

23. Huang DW, Sherman BT, Lempicki RA. Systematic and integrative analysis of large gene lists using DAVID bioinformatics resources. Nat Protoc 2009;4:44–57

24. Schweizer A, Kornfeld S, Rohrer J. Proper sorting of the cation-dependent mannose 6-phosphate receptor in endosomes depends on a pair of aromatic amino acids in its cytoplasmic tail. Proc Natl Acad Sci USA 1997;94:14471–14476

25. Tondera D, Czauderna F, Paulick K, Schwarzer R, Kaufmann J, Santel A. The mitochondrial protein MTP18 contributes to mitochondrial fission in mammalian cells. J Cell Sci 2005;118:3049–3059

26. Wicksteed B, Brissova M, Yan W, et al. Conditional gene targeting in mouse pancreatic β-cells: analysis of ectopic Cre transgene expression in the brain. Diabetes 2010;59:3090–3098

27. Tsuboi T, Ravier MA, Parton LE, Rutter GA. Sustained exposure to high glucose concentrations modifies glucose signaling and the mechanics of secretory vesicle fusion in primary rat pancreatic cCells. Diabetes 2006;55:1057–1065

28. Busby MA, Stewart C, Miller CA, Grzeda KR, Marth GT. Scotty: a web tool for designing RNA-Seq experiments to measure differential gene expression. Bioinformatics 2013;29:656–657
29. Satake E, Pezzolesi MG, Md Dom ZI, Smiles AM, Niewczas MA, Krolewski AS. Circulating miRNA profiles associated with hyperglycemia in patients with type 1 diabetes. Diabetes 2018;67:1013–1023
30. de Candia P, Spinetti G, Specchia C, et al. A unique plasma microRNA profile defines type 2 diabetes progression. PLoS One 2017;12:e0188980
31. Yi SW, Park S, Lee YH, Park HJ, Balkau B, Yi JJ. Association between fasting glucose and all-cause mortality according to sex and age: a prospective cohort study. Sci Rep 2017;7:8194
32. Kalwat MA, Cobb MH. Mechanisms of the amplifying pathway of insulin secretion in the β cell. Pharmacol Ther 2017;179:17–30
33. Gooding JR, Jensen MV, Dai X, et al. Adenylosuccinate is an insulin secretagogue derived from glucose-induced purine metabolism. Cell Rep 2015;13:157–167
34. Han G, Takahashi H, Murao N, et al. Glutamate is an essential mediator in glutamine-amplified insulin secretion. J Diabetes Investig 2021;12:920–930
35. Kato T, Shimano H, Yamamoto T, et al. Granuphilin is activated by SREBP-1c and involved in impaired insulin secretion in diabetic mice. Cell Metab 2006;4:143–154
36. Kreutzberger AJB, Kiessling V, Doyle CA, et al. Distinct insulin granule subpopulations implicated in the secretory pathology of diabetes types 1 and 2. eLife 2020;9:e62506
37. Mitchell RK, Hu M, Chabosseau PL, et al. Molecular genetic regulation of Slc30a8/ZnT8 reveals a positive association with glucose tolerance. Mol Endocrinol 2016;30:77–79
38. Brereton MF, Rohm M, Shimomura K, et al. Hyperglycaemia induces metabolic dysfunction and glycogen accumulation in pancreatic β-cells. Nat Commun 2016;7:13496
39. Yu CY, Yang CY, Rui ZL. MicroRNA-125b-5p improves pancreatic β-cell function through inhibiting JNK signaling pathway by targeting DACT1 in mice with type 2 diabetes mellitus. Life Sci 2019;224:67–75
40. Pohlmann R, Boeker MW, von Figura K. The two mannose 6-phosphate receptors transport distinct complements of lysosomal proteins. J Biol Chem 1995;270:27311–27318
41. Masini M, Bugliani M, Lupi R, et al. Autophagy in human type 2 diabetes pancreatic beta cells. Diabetologia 2009;52:1083–1086
42. Omar-Hmeadi M, Idevall-Hagren O. Insulin granule biogenesis and exocytosis. Cell Mol Life Sci 2021;78:1957–1970
43. Duroux-Richard I, Roubert C, Ammari M, et al. miR-125b controls monocyte adaptation to inflammation through mitochondrial metabolism and dynamics. Blood 2016;128:3125–3136
44. 0.02w?>Gu L, Zhu Y, Lin X, Li Y, Cui K, Prochownik EV. Amplification of glyceronephosphate O-acyltransferase and recruitment of USP30 stabilize DRP1 to promote hepatocarcinogenesis. Cancer Res 2018;78:5808–5819
45. Hennings TG, Chopra DG, DeLeon ER, et al. In vivo deletion of β-cell Drp1 impairs insulin secretion without affecting islet oxygen consumption. Endocrinology 2018;159:3245–3256
46. Twig G, Elorza A, Molina AJ, et al. Fission and selective fusion govern mitochondrial segregation and elimination by autophagy. EMBO J 2008;27:433–446
47. Wada J, Nakatsuka A. Mitochondrial dynamics and mitochondrial dysfunction in diabetes. Acta Med Okayama 2016;70:151–158
48. Wei LM, Sun RP, Dong T, et al. MiR-125b-2 knockout increases high-fat diet-induced fat accumulation and insulin resistance. Sci Rep 2020; 10:21969
49. Shannon P, Markiel A, Ozier O, et al. Cytoscape: a software environment for integrated models of biomolecular interaction networks. Genome Res 2003;13:2498–2504